

Seasonal predictability of summer melt ponds from winter sea ice surface temperature

Linda Thielke¹, Niels Fuchs^{2,4}, Gunnar Spreen¹, Bruno Tremblay³, Gerit
Birnbaum⁴, Marcus Huntemann¹, Nils Hutter^{5,4}, Polona Itkin⁶, Arttu Jutila⁴,
Melinda A. Webster⁷

¹Institute of Environmental Physics, University of Bremen, Bremen, Germany

²Center for Earth System Sustainability, Institute of Oceanography, University of Hamburg, Hamburg,
Germany

³Department of Atmospheric and Oceanic Sciences, McGill University, Montréal, Québec, Canada

⁴Alfred Wegener Institute, Helmholtz Centre for Polar and Marine Research, Bremerhaven, Germany

⁵Cooperative Institute for Climate, Ocean and Ecosystem Studies, University of Washington, Seattle,
WA, USA

⁶UiT The Arctic University of Norway, Tromsø, Norway

⁷University of Alaska Fairbanks, Fairbanks, AK, USA

Key Points:

- Winter warm surface temperature anomalies are co-located with melt pond locations in the following summer
- Warm anomalies appear in refrozen leads, potentially in refrozen melt ponds, and in troughs between ridges, due to thinner snow and ice
- We show the predictability of summer melt pond fraction from winter surface temperatures

Corresponding author: Linda Thielke, lthielke@iup.physik.uni-bremen.de

Abstract

Comparing helicopter-borne surface temperature maps in winter and optical orthomosaics in summer from the year-long Multidisciplinary drifting Observatory for the Study of Arctic Climate (MOSAiC) expedition, we find a strong geometric correlation between warm anomalies in winter and melt pond location the following summer. Warm anomalies are attributed to thinner snow and ice on level ice compared to the deformed ice in the surroundings or refrozen leads with only newly formed, thin ice. Warm surface temperature anomalies in January were 0.3 K to 2.5 K warmer on sea ice that later formed melt ponds. A one-dimensional steady-state thermodynamic model shows that the observed surface temperature differences are in line with the observed ice thickness and snow depth. We demonstrate the potential of seasonal prediction of summer melt pond location and coverage from winter surface temperature observations. A threshold-based classification achieves a correct classification for 41% of the melt ponds.

Plain Language Summary

We compare winter surface temperatures from an infrared camera with summer photographs of sea ice with melt ponds. The datasets were recorded from a helicopter during the Multidisciplinary drifting Observatory for the Study of Arctic Climate (MOSAiC) expedition. Melt ponds form on sea ice in summer when the snow melts and water accumulates in the lower locations on the ice floes. Melt ponds are very important for the Arctic energy budget because they strongly change the sea ice brightness and thus the amount of solar energy absorbed by the ice. We find surface characteristics with similar size and location between warmer areas in winter and the location of melt ponds in summer. For a better process understanding, we calculate the surface temperature with a simple model and find that the warm temperature anomalies are due to thinner ice and snow. Stronger warm temperature anomalies appear in new cracks in the ice which are covered with newly formed, thin ice. With a temperature-based classification, we are able to estimate the summer melt pond coverage.

1 Introduction

Melt ponds on Arctic sea ice are an important component of the summer energy budget (e.g., Nicolaus et al., 2012). Melt ponds contribute to the ice–albedo feedback by lowering the surface albedo (e.g., Curry et al., 1995; Light et al., 2022) and thus influencing the radiation balance of the Arctic sea ice (e.g., Perovich et al., 2011). For autumn, Anhaus et al. (2021) showed that melt ponds are influencing light transmission. The preconditioning of melt ponds can be partly explained by ice topography (e.g., Flocco et al., 2015; Polashenski et al., 2012), predominately for deformed second-year ice (SYI), or snow dunes and snow accumulations (Petrich et al., 2012; Polashenski et al., 2012), mainly on level first-year ice (FYI). Additional factors for melt pond preconditioning are ice permeability and pond hydrology (Eicken et al., 2002, 2004). There are distinct differences between melt ponds on level or deformed ice. The melt pond location and size are controlled by the topography of deformed ice while on level ice melt ponds can cover large areas (Webster et al., 2022). The ice topography, induced by ridges or leads, are either remnant from the previous seasons’ dynamic events or can be newly created due to ice dynamics and/or snow accumulation (Polashenski et al., 2012). Also, refrozen melt ponds can have a lower ice surface elevation and ice thickness compared to the surroundings. There are still large uncertainties in models to predict melt ponds, especially their parameterization of size, depth, and effect on light transmission (Light et al., 2008; Flocco et al., 2012; Webster et al., 2022). Small-scale processes are very important (Vihma et al., 2014), but challenging to observe and analyze. Although higher resolution thermal infrared satellites exist, they are used only in lower latitudes like Landsat 8. Therefore, we strive to gain more knowledge from our high resolution helicopter surface tempera-

72 ture maps in winter as a prediction of next summer’s melt pond areal extent because sur-
 73 face temperatures are sensitive to the ice and snow topography. We can connect the phys-
 74 ical understanding of melt ponds across the seasons (predictability) and how the warm
 75 anomalies appear during winter (preconditioning). From this, we provide knowledge on
 76 how to accomplish a better representation of melt ponds in models.

77 Specifically, we present a case study from the observations of the MOSAiC expe-
 78 dition from September 2019 to October 2020. RV *Polarstern* (AWI, 2017) drifted with
 79 the sea ice from the northern Laptev Sea towards the Fram Strait. A large suite of mea-
 80 surements was carried out continuously over the same ice area from October to July (Nico-
 81 laus et al., 2022; Shupe et al., 2022; Rabe et al., 2022). This study combines helicopter-
 82 borne thermal infrared (TIR) imaging with optical orthomosaics and topography data
 83 from an airborne laser scanner (ALS), snow and ice thickness measurements from ground-
 84 based transects, as well as atmospheric measurements of temperature, wind speed, and
 85 longwave radiation.

86 We approximate the location and area of summer melt ponds using the preceding
 87 winter’s sea ice surface temperature data. Based on the comparison of the helicopter-
 88 borne maps, we find warm surface ice temperature anomalies in winter at the location
 89 of the next summer’s melt ponds. We use a simple one-dimensional thermodynamic model
 90 to identify the drivers of the warm anomalies. To conclude, we discuss the potential, lim-
 91 itations, and implications of these novel findings to use them for the improvement of mod-
 92 elling and new ideas for high resolution satellite remote sensing.

93 2 Data and Methods

94 We investigate the same sea ice area several months apart and perform a one-to-
 95 one comparison between summer and winter. The main data sets are recorded with helicopter-
 96 borne imaging: TIR for the polar night (Thielke et al., 2022b) and optically during the
 97 polar day. The rich additional MOSAiC datasets are ideally suited to constrain the phys-
 98 ical conditions during the seasons.

99 2.1 Study area

100 The study area ($1.3 \text{ km} \times 1.3 \text{ km}$) consists of level FYI as well as deformed SYI that
 101 survived the previous summer melt (Krumpen et al., 2020). The remnant of the MO-
 102 SAiC floe observed in summer during leg 4, was during winter (legs 1 and 2) in the de-
 103 formed ice area at the edge of the main sampling sites (about 1.5 km distance from RV
 104 *Polarstern*). The area of the MOSAiC floe in summer is marked by the red polygon in
 105 Figure 1. Additional information about the aerial surface temperatures is provided in
 106 the Supporting Information (Subsection "Warm temperature anomalies").

107 2.2 Optical orthomosaic in summer

108 We use the optical orthomosaic from 30 June 2020 as the ground truth for the melt
 109 pond coverage on the MOSAiC floe during summer. The orthomosaic, a composite of
 110 aerial RGB images, clearly illustrates the melt ponds as darker grayish-blueish areas in
 111 contrast to white ice and the almost black open water around the floe. These optical dif-
 112 ferences are used in a supervised classification algorithm developed for aerial images of
 113 sea ice to semantically divide the orthomosaic into surface type class objects. To reduce
 114 the impact of noise on pixel level, the minimum size of the resulting *snow/ice*, *pond*, *sub-*
 115 *merged ice* and *open water* objects is limited to 100 pixels at a pixel area of 0.25 m^2 (more
 116 information: <https://gitlab.awi.de/nifuchs/pasta-ice/>). The estimated error is
 117 below $\pm 2\%$ for the derived pond fraction.

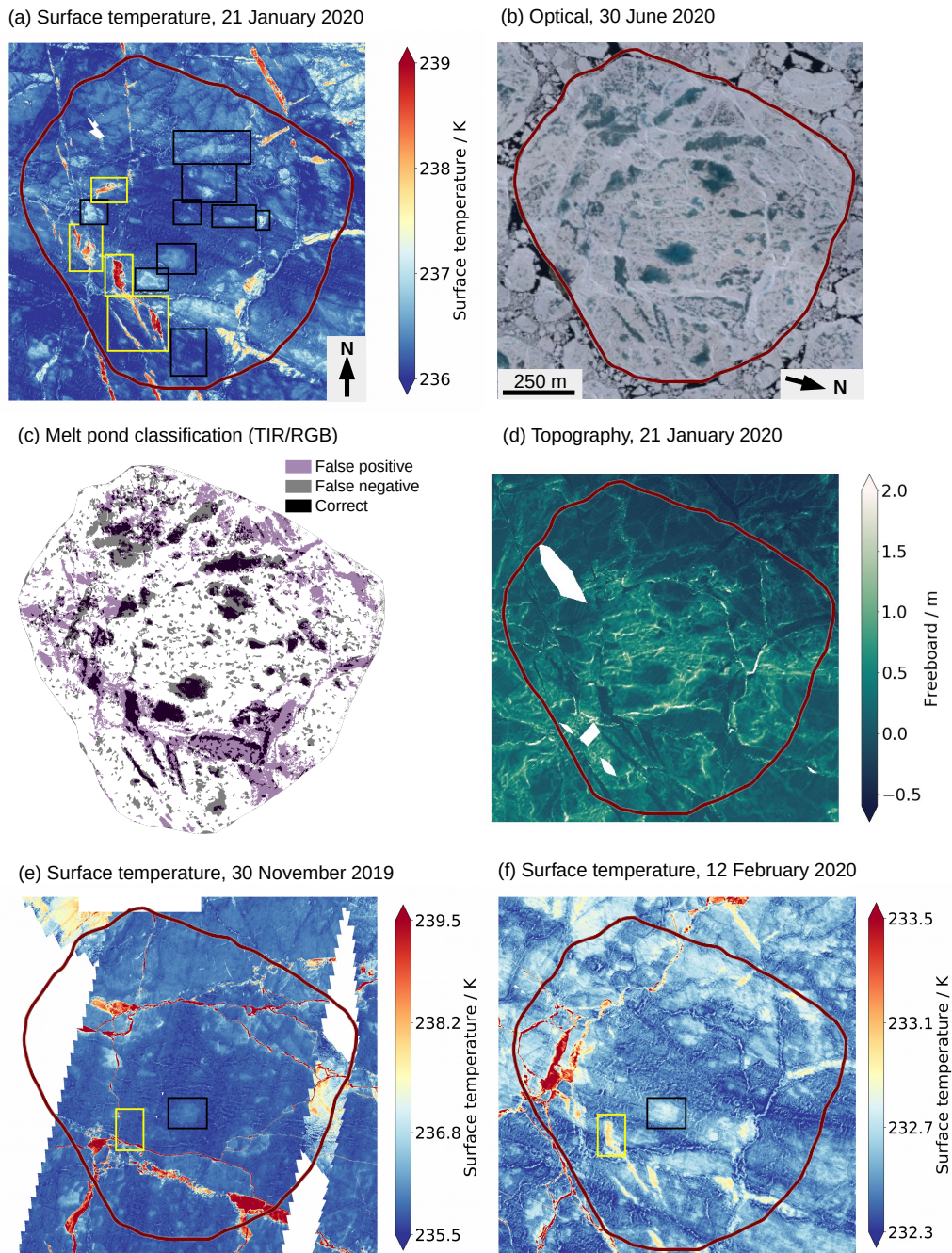


Figure 1. (a) Surface temperature map (TIR) on 21 January 2020 with the boxes indicating the warm anomalies. Yellow boxes are refrozen leads (RL) and black boxes are topography controlled (TC). (b) Optical orthomosaic (RGB) from 30 June 2020 showing the melt ponds as grayish-blueish colors. (c) Overlay of melt pond classification based on a surface temperature threshold on 21 January 2020 and based on RGB classification on 30 June 2020 with fractions of 26% and 22%, respectively. [Purple: only classified by TIR (false positive); Gray: only classified by RGB (false negative); Black: classified in both data (correct).] (d) Freeboard map showing snow surface topography on 21 January 2020. Surface temperatures on (e) 30 November 2019 and (f) 12 February 2020 (note that the colorbar is different for better visibility). The two boxes are indicating the RL and TC cases highlighted in the study. The outline of the summer ice floe as a red polygon for reference.

118 2.3 Aerial surface temperatures in winter

119 The surface temperature maps are based on helicopter-borne TIR imaging, per-
 120 formed with the VarioCam HD head 680 camera with a brightness temperature preci-
 121 sion of 0.02 K and accuracy of 1 K (Thielke et al., 2022b). We use gridded surface tem-
 122 peratures at 1 m horizontal resolution. We focus on data from 21 January 2020 that con-
 123 tained numerous distinct thermal features. For comparison, we show the warm anom-
 124 lies in the flight on 30 November 2019 and 12 February 2020 (Figure 1 e,f).

125 2.4 Definition of warm anomalies

126 There are two approaches used to define the warm anomalies on the temperature
 127 map of 21 January 2020. The first method is more specific to each of the 13 identified
 128 cases (boxes in Figure 1 a), which is more applicable to the meter scale, while the other
 129 is a temperature threshold for identifying warm patches across the 1.5 km floe to per-
 130 form a melt pond classification.

131 1) Based on the "ground truth" of the summer optical orthomosaic, we manually
 132 defined 13 warm anomalies in the surface temperature map from 21 January 2020. In
 133 each box, we analyze two manually selected temperature cross-sections covering both the
 134 warm anomaly and the surroundings (Figure 2). We further manually classify the cross-
 135 sections in an "anomaly" and "surrounding" part. The temperatures of the two classes
 136 are averaged while the transitions between the two are not analyzed. From that, the sur-
 137 face temperature difference $\Delta T_{s,obs}$ between the two classes is calculated. For the pre-
 138 cise definition of the melt pond location, we need a manual classification because the larger
 139 scale spatial variability is in the same range as the temperature difference of the warm
 140 anomalies.

141 2) To retrieve the melt pond fraction of the whole study area we apply one fixed
 142 temperature threshold of 236.35 K to the aerial surface temperature to classify it in melt
 143 ponds and ice. The threshold is manually selected by tuning for the most reasonable out-
 144 come of the temperature classification compared to the optical ground truth. From this,
 145 we can investigate the performance of the winter melt pond classification based on sur-
 146 face temperatures. The classification is very sensitive to the threshold because changes
 147 in 0.05 K steps already resulted in different classified areas. We compare the tempera-
 148 ture classification to the classified orthomosaic in terms of location and fraction. Both
 149 maps are manually superimposed to achieve the best overlap (Figure 1 c).

150 2.5 Surface topography

151 The surface topography of the snow surface is retrieved from the ALS, which was
 152 operated in the helicopter, parallel to the TIR camera. The freeboard of the snow sur-
 153 face can be used to evaluate the topography of the areas of the warm anomalies and their
 154 surroundings as an additional variable for the winter conditions.

155 2.6 Snow and ice conditions

156 To evaluate the snow and ice conditions, we use measurements along a transect (called
 157 "Northern Loop"), which were taken over deformed ice close to our study data. More
 158 information about the transect location can be found in Figure 2 of Nicolaus et al. (2022).
 159 We discriminate between level and deformed ice based on the roughness determined from
 160 the 50 m running mean and standard deviation of the ice thickness, same as in Itkin et
 161 al. (2022, in review). The level ice thickness is capped at 2 m (assumed thermodynam-
 162 ical growth limit). The standard deviation has to be less than 0.2 m for level ice and higher
 163 than 0.6 m for deformed ice. The values of snow and ice thickness measured at the spe-

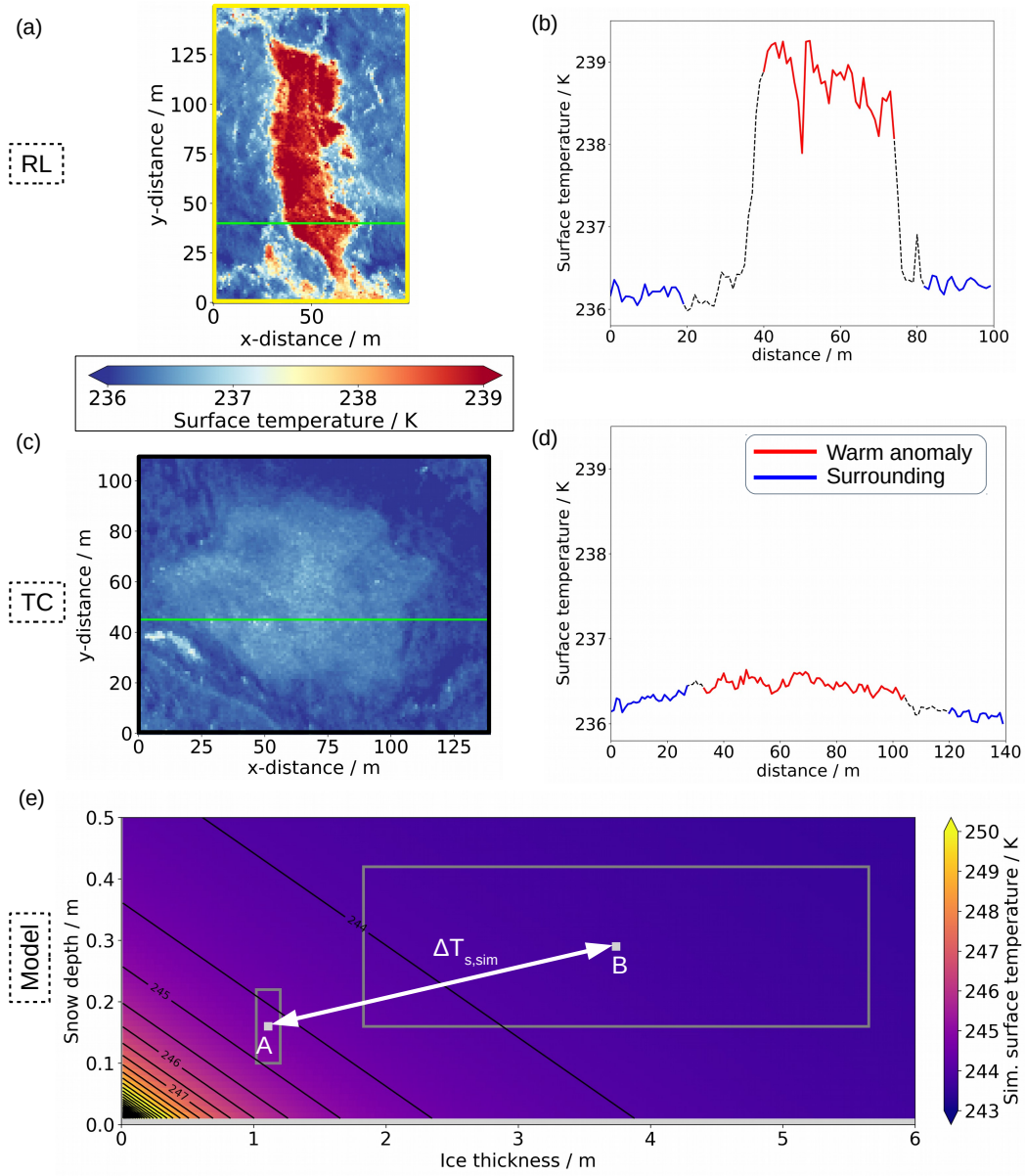


Figure 2. (a,b) Case example for RL (Box 3). (c,d) Case example for TC (Box 5). (a,c) Surface temperature map of the box with a cross-section (green line). (b,d) Surface temperature along the cross-section with the classification of the warm anomaly (red) and the surroundings (blue). (e) Simulated surface temperature (colored) for ice thickness versus snow depth on 21 January 2020. The black contour lines show the surface temperature step size of 0.5 K. Point "A": typical for the level ice in the warm anomalies; point "B": typical for deformed ice in the surroundings. The boxes are defined based on the mean and standard deviation of the snow and ice thickness.

164 cific transect days (transects were performed monthly to bi-weekly) are fitted polyno-
165 mially and retrieved for 21 January 2020.

166 2.7 Thermodynamic sea ice model

167 We implement a one-dimensional steady-state thermodynamic sea ice model to in-
168 vestigate the sensitivity of the surface temperature to changes in snow and ice thickness
169 as well as atmospheric parameters, i.e., 2 m air temperature, 10 m wind speed, and down-
170 welling longwave radiation.

171 The surface heat budget is defined as (Shokr & Sinha, 2015):

$$F_{\text{LW,down}} - F_{\text{LW,up}} + F_{\text{cond}} - F_{\text{sens}} = 0, \quad (1)$$

172 where $F_{\text{LW,down}}$ and $F_{\text{LW,up}}$ are the downwelling and upwelling longwave radiation, F_{cond}
173 the conductive heat flux, and F_{sens} the sensible heat flux. Fluxes towards the surface are
174 considered positive. Shortwave radiation is not relevant during winter and the latent heat
175 flux is negligibly small. With the one-dimensional model, we do not consider lateral heat
176 fluxes which we assume to be negligible.

177 Linearizing $F_{\text{LW,up}}$ using Taylor expansion, the simulated surface temperature $T_{\text{s,sim}}$
178 is:

$$T_{\text{s,sim}} = \frac{F_{\text{LW,down}} - a + T_{\text{w}} d + c u T_{\text{a}}}{b + c u + d}, \quad \text{where } d = \left(\frac{h_{\text{i}}}{k_{\text{i}}} + \frac{h_{\text{s}}}{k_{\text{s}}}\right)^{-1}. \quad (2)$$

179 T_{w} is the sea water temperature at freezing point, c is the combined sensible transfer co-
180 efficient, u the wind speed, h_{i} is the ice thickness, h_{s} is the snow depth, k_{i} and k_{s}
181 are the thermal conductivity of ice and snow respectively, a and b are the coefficients of lin-
182 earization.

183 The model is forced with atmospheric data from the meteorological tower on the
184 floe and longwave radiation from a radiation station, both at the recording time of the
185 surface temperatures. The snow and ice thicknesses of level and deformed ice are taken
186 from the transect data. There can be absolute differences in surface temperature between
187 our observations of TIR surface temperatures and the simulated physical temperature.
188 However, this does not impact relative differences across the floe, which are most impor-
189 tant here. The full model descriptions and input parameters can be found in the Sup-
190 plementary Information (Subsection "Details on the thermodynamic model").

191 3 Results

192 3.1 Warm anomaly types

193 Comparing the melt ponds from the optical orthomosaic (Figure 1 b) with warm
194 anomalies of the surface temperature map in winter (Figure 1 (a)) we find clear simi-
195 larities in location and shape. Although we do not have any visual appearance of melt
196 ponds in winter and spring, we can detect anomalies, that will become melt ponds in sum-
197 mer, with our thermal observations in winter (boxes in Figure 1 a; numbers in Figure S1 b
198 in Supporting information).

199 Based on the observed temperature contrasts and their physical explanation, we
200 define and manually select two types of these warm anomalies:

- 201 a) Refrozen leads (RL): newly formed, thin ice in between thicker ice, showing strong
202 positive temperature anomalies.
- 203 b) Topography controlled (TC): level ice surrounded by deformed ice, showing weak
204 positive temperature anomalies.

205 The refrozen leads can be identified easily by their elongated shape and higher sur-
 206 face temperatures due to thinner ice formed after a recent dynamic event. They have
 207 a lower surface elevation than the surroundings and potentially collect more snow which
 208 favors melt water collection in summer.

209 Besides the correlation with the optical orthomosaic, we find the same for areas of
 210 low elevation in the aerial topography map from the ALS (Figure 1 d). Thus, warm anoma-
 211 lies often have thinner ice and snow compared to the surroundings of deformed ice with
 212 increased freeboard and surface roughness. Based on this topography data, we can de-
 213 termine topography controlled melt ponds although they show a comparatively small tem-
 214 perature difference. Many of the TC anomalies already have the shape of melt ponds and
 215 thus potentially were melt ponds already the summer before.

216 3.2 Local temperature differences

217 Here, we show the results from the manual classification in each box. The surface
 218 temperature differences of the two warm anomaly types on 21 January vary between 0.3 K
 219 and 2.5 K. We find a connection between the temperature difference and the type of anoma-
 220 lies. For the RL (four anomalies), we have a higher temperature difference between 1.7 K
 221 and 2.5 K (median=2.0 K, std=0.33 K), while the TC anomalies (nine anomalies) have
 222 a temperature difference between 0.3 K and 0.7 K (median=0.4 K, std=0.17 K).

223 For simplicity, we focus on one case of each type, RL and TC, because they have
 224 a well-distinguishable temperature anomaly. In Figure 2, we show the temperature maps
 225 for one RL-case ($\Delta T_{\text{obs}} = 2.5$ K) and one TC-case ($\Delta T_{\text{obs}} = 0.3$ K) as well as the tem-
 226 peratures of the cross-sections. The cross-sections are classified into warm anomaly (red)
 227 and surroundings (blue). Looking at all helicopter TIR data we see that RL only appear
 228 after the end of December and then the surface temperature difference decrease due to
 229 ice growth and potential snow accumulation from 11.8 K to 0.5 K. For TC there is no
 230 trend with time while it varies between 0.2 K and 1.3 K. The different stages of the warm
 231 anomalies on 30 November 2019 and 12 February 2020 are displayed in Figure 1 e and f.
 232 Temperature differences of all 13 warm anomalies on 21 January and in two cases for all
 233 10 helicopter flights between November and February are listed in the Supporting In-
 234 formation (Subsection "Warm temperature anomalies").

235 3.3 Comparison of observations and thermodynamic model

236 We compare the warm anomalies from the TIR observation on 21 January with sim-
 237 ulated surface temperature differences, calculated with a steady state one-dimensional
 238 thermodynamic model (Subsection 2.7) to understand better what is causing the warm
 239 winter anomalies. The lower temperature contrast of TC has to be investigated in more
 240 detail while for the RL cases it is clear that the newly formed, thinner ice causes the larger
 241 temperature differences. Thus, we focus on the TC melt ponds on 21 January 2020

242 We determine the snow depth and ice thickness for level and deformed ice, which
 243 are representative of the warm anomalies and of the surroundings. Snow depth and ice
 244 thickness from the transect data represent the spatial variability of the study area and
 245 show a snow depth of $0.16 \text{ m} \pm 0.06 \text{ m}$ for level (A) and $0.29 \text{ m} \pm 0.13 \text{ m}$ for deformed
 246 ice (B) (Figure 2 e). The ice thickness is $1.11 \text{ m} \pm 0.09 \text{ m}$ for level ice (A) and $3.74 \text{ m} \pm 1.91 \text{ m}$
 247 for deformed ice (B). We implement two regimes of snow depth and ice thickness. The
 248 simulated mean temperature difference $\Delta T_{\text{s,sim}}$ between the warm anomaly (level) and
 249 surroundings (deformed) is 0.88 K with a spread from 0.09 K to 1.47 K (Figure 2 e) while
 250 0.30 K to 0.70 K is observed (Subsection 3.2).

251 Thus, the thermodynamic model slightly overestimates the temperature anomaly.
 252 The simulated temperature difference using the same snow depth for level and deformed
 253 ice (0.23 m) would be 0.59 K. Therefore, the effect of variable snow depth accounts for

254 0.29 K of the 0.88 K in our simulation. But this snow depth variability is quite uncer-
 255 tain based on our limited amount of measurements.

256 3.4 Temperature-based melt pond classification

257 The threshold-based TIR classification is able to approximate the next summer melt
 258 pond fraction of an ice floe. With a temperature threshold of 236.35 K, applied to the
 259 surface temperature map on 21 January 2020, we derive a melt pond fraction of 26% (Fig-
 260 ure 1 c). This is slightly higher than the fraction of 22% for the optical classification on
 261 30 June 2020. With the ponds expanding after the first drainage event in mid-July, how-
 262 ever, the optical observations also show a higher fraction of 24% on 22 July 2020. Thus,
 263 we are able to partly replicate the summer melt pond classification, already six months
 264 in advance, and can be used as a seasonal prediction tool for melt ponds. The shortcom-
 265 ings are the uncertainties on level FYI as well as that we are missing smaller melt ponds
 266 (melt pond size distribution follows a power law (Popović et al., 2018; Huang et al., 2016)).
 267 Also the high spatial variability of the surface temperature influences the classification
 268 which is sensitive to small changes in the threshold. The temperature classification per-
 269 formed correctly for 41% of the optical classified ponds (Figure 2 c). The remaining 59%
 270 are not classified although in summer melt ponds are present (false negative). In rela-
 271 tion to the whole surface area of the floe, the fraction of false positive (17% of the floe)
 272 and false negative (13% of the floe) are in the same order of magnitude. Therefore, the
 273 overall melt pond fraction is similar for the TIR and optical classification, which can be
 274 a coincidence. However, as 41% of the summer melt ponds are correctly identified in the
 275 winter TIR data that number is the approximate performance of the winter to summer
 276 melt pond predictability.

277 4 Discussion

278 Studies about melt pond properties (Huang et al., 2016) and photogrammetry of
 279 the sea ice topography (Divine et al., 2016) using optical data are limited to the sum-
 280 mer season. Helicopter-borne ALS data, available in summer and winter, were also used
 281 to explore the role of surface roughness for melt pond presence (Webster et al., 2022).
 282 With high resolution winter surface temperatures, we add an additional data source for
 283 a better understanding of melt pond characteristics outside the summer season. We show
 284 for the first time that melt pond locations can be already seen in winter temperature anoma-
 285 lies due to the thermodynamic properties of snow and sea ice.

286 We find areas of refrozen leads or level ice with thinner snow at the location of the
 287 anomalies and deformed ice in the surroundings. This is reasonable because areas of low
 288 elevation tend to turn into melt ponds (Polashenski et al., 2012). The ice topography
 289 and snow variability align with the findings of Scott and Feltham (2010) and Holland
 290 et al. (2012). Two modes, corresponding to level and deformed ice as found in the tran-
 291 sect ice thickness (1.11 m and 3.74 m), are also visible in the ice thickness transect per-
 292 formed on 07 January 2020 over parts of the study area (Figure S2 in Supplementary
 293 Information). When we zoom into the study area these modes are represented also by
 294 the ALS freeboard. We can identify modes for each of the anomalies which are below
 295 the surroundings (Figure S3 in Supplementary Information). This strengthens our as-
 296 sumptions for the two ice thickness regimes in the thermodynamic model. Previous stud-
 297 ies stated that snow plays an important role for melt pond formation (Scott & Feltham,
 298 2010; Petrich et al., 2012). In our study, we can show that the important factor snow
 299 can be linked to the ice topography while thinner snow over level ice favors the warm
 300 temperature anomalies.

301 The presence of some TC melt ponds is likely due to re-frozen melt ponds from the
 302 previous summer. We have no data from the previous season to prove that but the size
 303 of the warm anomalies hint in that direction. Also, many re-frozen melt ponds were ob-

304 served on the MOSAiC floe. For example, Itkin et al. (2022, in review) show that melt
305 ponds were present on the MOSAiC floe in the previous summer. The re-appearance of
306 melt ponds at the previous season's location was already mentioned before in the con-
307 text of the Surface Heat Budget of the Arctic Ocean (SHEBA) expedition (Eicken et al.,
308 2001). In one case (Box 4) we find a warmer circle around a colder middle part, which
309 could indicate a bottom-up melt pond from last summer. The trough of the previous melt
310 pond could serve as the meltwater collection location. This then serves as a seed for the
311 next season because melt ponds tend to reappear at the previous summer's location (Eicken
312 et al., 2001).

313 To simulate the surface temperature, we assumed a commonly used value of snow
314 thermal conductivity ($k_s=0.30 \text{ W m}^{-1} \text{ K}^{-1}$, Bitz and Lipscomb (1999)). The model re-
315 sults are sensitive to the thermal conductivity and this could be one reason why our re-
316 sults are slightly overestimated. The investigation of the thermal conductivity is an im-
317 portant but large topic itself and out of the scope of this study.

318 The threshold-based temperature melt pond classification could be applied in a model
319 but would need to be adjusted. The surface temperature depends on the air tempera-
320 ture, and the surface temperature anomalies vary with atmospheric parameters like wind
321 speed. The comparison to the optical classification shows that a single threshold has still
322 some problems to classify melt pond locations correctly. 41% of the summer locations
323 are correctly predicted and thus the majority was not. This shows the limit of our pre-
324 dictability: while 41% is still a useful prediction we cannot expect to identify all sum-
325 mer melt ponds already in winter. However, our comparison does not take sea ice dy-
326 namics as well as snow accumulation and redistribution between winter and summer into
327 account. Thus some of the mismatches might be due to that and can partly explain the
328 good match of the classified overall melt pond fraction of 26% in winter and 22% (max-
329 imum 24%) in summer.

330 Melt pond schemes in regional and climate models could benefit from our findings:
331 melt ponds should be tracked in models throughout the whole year and not only in sum-
332 mer. This increases the potential for predictability. So far the ice and snow topography
333 is not represented sufficiently in General Circulation Models (e.g., Flocco et al., 2012).
334 But in this study, we show how important the ice topography and roughness are for melt
335 pond formation, already in winter.

336 Until now, refrozen leads were not considered as an indicator of melt ponds. The
337 refrozen leads can add potential areas for next summer's melt pond formation. Here, we
338 can show that a proper representation of lead formation and ice dynamics is necessary
339 to improve the melt pond predictability. Thus, the area of refrozen leads explains a part
340 of the melt pond fraction of the following summer. While sea ice is becoming thinner,
341 it becomes more dynamic, and more leads can form. Thus, there is potential for an in-
342 creased area of melt ponds in the future, which can alter the albedo of sea ice.

343 Further, TIR remote sensing data can help to support the findings presented here.
344 Satellites instead of helicopter surveys would be an ideal tool to cover larger areas. How-
345 ever, so far, higher resolution TIR satellite remote sensing is performed only in lower lat-
346 itudes, while we show their potential benefits for the whole Arctic. Nevertheless, their
347 current spatial resolution of about 100 m is still not sufficient to resolve the warm anoma-
348 lies, which are usually smaller. This study should motivate to implement high resolu-
349 tion TIR satellite-based observations, like the upcoming Copernicus LSTM mission with
350 30 m resolution (Koetz et al., 2018), to resolve small-scale physical processes on a wider
351 scale and extend their coverage to polar regions.

5 Conclusion

We show that warm surface temperature anomalies over sea ice in winter can be co-located with summer melt ponds of the following summer. We define two different types of warm anomalies: refrozen leads and topography controlled melt ponds. The warm anomalies of the topography controlled melt ponds are characterized by level ice compared to the deformed surroundings, which means thinner snow and ice for the warm anomalies. With a thermodynamic model, we are able to replicate (with a slight ΔT overestimation) the observed surface temperature difference based on observed snow and ice thickness difference, and atmospheric parameters. Thus, we can fully attribute the warm anomaly to the ice and snow cover (and not, e.g., wind-driven effects), which eventually also affects later pond formation. Based on a simple threshold-based classification, we are able to use high resolution surface temperature in winter as a seasonal prediction tool for the summer melt pond fraction. The winter prediction of the observed summer melt pond fraction agrees within their uncertainty and 41% of the summer melt pond locations are identified correctly.

As Scott and Feltham (2010) and Landy et al. (2014) point out, there is a need for a better understanding of physical processes influencing melt pond formation and evolution which is driven by meteorological events, ice dynamics, and thermodynamics. The relationships between winter ice surface temperature and melt pond development found here, can serve the development of improved melt pond parameterizations in regional and climate models. They should track re-frozen lead locations throughout the winter and take pond formation in re-frozen leads into account to simulate a more realistic melt pond distribution. As shown in this study, there is a large potential for high resolution TIR data to study small-scale properties of sea ice, either from airborne platforms like here or hopefully in future satellite missions.

Data availability

- Optical orthomosaics: under submission to PANGAEA
- Surface temperature maps: Thielke et al. (2022a)
- Freeboard maps: under submission to PANGAEA
- Atmospheric parameter: Cox et al. (2021) [updated version used]
- Radiation: under submission to PANGAEA
- Transect: Hendricks et al. (2022) [ice thickness], Itkin et al. (2021) [snow depth]

Contributions

Conceptualization: LT, NF, GS
 Methodology: LT, GS, BT
 Data contribution: LT, NF, GS, GB, MH, NH, PI, AJ, MAW
 Discussion: LT, NF, GS, BT, GB, MH, PI, MAW
 Analysis: LT, NF, BT
 Writing original draft: LT
 Review and editing: all authors

Acknowledgments

This work was supported by the German Ministry for Education and Research (BMBF) as part of the International Multidisciplinary drifting Observatory for the Study of the Arctic Climate (grant MOSAiC20192020), NiceLABpro (grant 03F0867A), and IceSense (grants 03F0866B and 03F0866A). We acknowledge the support by the Deutsche Forschungsgemeinschaft (DFG) through the International Research Training Group IRTG 1904 Arc-Train (grant 221211316), and the MOSAiCmicrowaveRS project (grant 420499875). PI was supported by Research Council of Norway (SIDRIFT, grant 287871). MAW conducted

400 this work under the National Aeronautics and Space Administration’s New Investiga-
 401 tor Program in Earth Science (80NSSC20K0658). We thank all persons involved in the
 402 expedition of the Research Vessel Polarstern during MOSAiC in 2019-2020 (AWI_PS122_00),
 403 and especially, HeliService and their pilots (Nixdorf et al., 2021). We also thank for the
 404 discussion and support around this project: Philipp Anhaus, Larysa Istomina, Felix Lin-
 405 hardt, Niklas Neckel, and Marcel Nicolaus.

406 References

- 407 Anhaus, P., Katlein, C., Nicolaus, M., Hoppmann, M., & Haas, C. (2021). From
 408 bright windows to dark spots: Snow cover controls melt pond optical proper-
 409 ties during refreezing. *Geophysical Research Letters*, *48*(23), e2021GL095369.
 410 doi: <https://doi.org/10.1029/2021GL095369>
- 411 AWI. (2017). Polar Research and Supply Vessel POLARSTERN operated by the
 412 Alfred-Wegener-Institute. *Journal of large-scale research facilities*, *3*. (Alfred-
 413 Wegener-Institut Helmholtz-Zentrum für Polar- und Meeresforschung) doi:
 414 <http://dx.doi.org/10.17815/jlsrf-3-163>
- 415 Bitz, C. M., & Lipscomb, W. H. (1999). An energy-conserving thermody-
 416 namic model of sea ice. *Journal of Geophysical Research: Oceans*, *104*(C7),
 417 15669–15677. doi: <https://doi.org/10.1029/1999JC900100>
- 418 Cox, C., Gallagher, M., Shupe, M., Persson, O., Solomon, A., et al. (2021). *10-*
 419 *meter (m) meteorological flux tower measurements (Level 1 Raw), Mul-*
 420 *tidisciplinary Drifting Observatory for the Study of Arctic Climate (MO-*
 421 *SAiC), central Arctic, October 2019 - September 2020.* Arctic Data Center.
 422 <https://doi.org/10.18739/A2VM42Z5F>.
- 423 Curry, J. A., Schramm, J. L., & Ebert, E. E. (1995). Sea Ice-Albedo Climate
 424 Feedback Mechanism. *Journal of Climate*, *8*(2), 240 - 247. Retrieved from
 425 [https://journals.ametsoc.org/view/journals/clim/8/2/1520-0442_1995_](https://journals.ametsoc.org/view/journals/clim/8/2/1520-0442_1995_008_0240_siacfm_2_0_co_2.xml)
 426 [_008_0240_siacfm_2_0_co_2.xml](https://journals.ametsoc.org/view/journals/clim/8/2/1520-0442_1995_008_0240_siacfm_2_0_co_2.xml) doi: 10.1175/1520-0442(1995)008<0240:
 427 SIACFM>2.0.CO;2
- 428 Divine, D. V., Pedersen, C. A., Karlsen, T. I., Aas, H. F., Granskog, M. A., Hudson,
 429 S. R., & Gerland, S. (2016). Photogrammetric retrieval and analysis of small
 430 scale sea ice topography during summer melt. *Cold Regions Science and Tech-*
 431 *nology*, *129*, 77–84. doi: <https://doi.org/10.1016/j.coldregions.2016.06.006>
- 432 Eicken, H., Grenfell, T., Perovich, D., Richter-Menge, J., & Frey, K. (2004). Hy-
 433 draulic controls of summer Arctic pack ice albedo. *Journal of Geophysical Re-*
 434 *search: Oceans*, *109*(C8). doi: <https://doi.org/10.1029/2003JC001989>
- 435 Eicken, H., Krouse, H., Kadko, D., & Perovich, D. (2002). Tracer studies of path-
 436 ways and rates of meltwater transport through arctic summer sea ice. *Journal*
 437 *of Geophysical Research: Oceans*, *107*(C10), SHE-22. doi: [https://doi.org/10.](https://doi.org/10.1029/2000JC000583)
 438 [.1029/2000JC000583](https://doi.org/10.1029/2000JC000583)
- 439 Eicken, H., Tucker, W., & Perovich, D. (2001). Indirect measurements of the
 440 mass balance of summer arctic sea ice with an electromagnetic induction tech-
 441 nique. *Annals of Glaciology*, *33*, 194–200. doi: [https://doi.org/10.3189/](https://doi.org/10.3189/172756401781818356)
 442 [172756401781818356](https://doi.org/10.3189/172756401781818356)
- 443 Flocco, D., Feltham, D. L., Bailey, E., & Schroeder, D. (2015). The refreezing
 444 of melt ponds on Arctic sea ice. *Journal of Geophysical Research: Oceans*,
 445 *120*(2), 647–659. doi: <https://doi.org/10.1002/2014JC010140>
- 446 Flocco, D., Schroeder, D., Feltham, D. L., & Hunke, E. C. (2012). Impact of melt
 447 ponds on Arctic sea ice simulations from 1990 to 2007. *Journal of Geophysical*
 448 *Research: Oceans*, *117*(C9). doi: <https://doi.org/10.1029/2012JC008195>
- 449 Hendricks, S., Itkin, P., Ricker, R., Webster, M., von Albedyll, L., Rohde, J., et
 450 al. (2022). *GEM-2 quicklook total thickness measurements from the 2019-*
 451 *2020 MOSAiC expedition.* PANGAEA. [https://doi.pangaea.de/10.1594/](https://doi.pangaea.de/10.1594/PANGAEA.943666)
 452 [PANGAEA.943666](https://doi.pangaea.de/10.1594/PANGAEA.943666).

- 453 Holland, M. M., Bailey, D. A., Briegleb, B. P., Light, B., & Hunke, E. (2012). Im-
 454 proved sea ice shortwave radiation physics in CCSM4: The impact of melt
 455 ponds and aerosols on Arctic sea ice. *Journal of Climate*, 25(5), 1413–1430.
 456 doi: <https://doi.org/10.1175/JCLI-D-11-00078.1>
- 457 Huang, W., Lu, P., Lei, R., Xie, H., & Li, Z. (2016). Melt pond distribution and
 458 geometry in high Arctic sea ice derived from aerial investigations. *Annals of*
 459 *Glaciology*, 57(73), 105–118. doi: <https://doi.org/10.1017/aog.2016.30>
- 460 Itkin, P., et al. (2022, in review). Sea ice and snow mass balance from transects in
 461 the MOSAiC Central Observatory. *Elem Sci Anth*.
- 462 Itkin, P., Webster, M., Hendricks, S., Oggier, M., Jaggi, M., Ricker, R., et al. (2021).
 463 *Magnaprobe snow and melt pond depth measurements from the 2019-2020*
 464 *MOSAiC expedition*. PANGAEA. [https://doi.pangaea.de/10.1594/](https://doi.pangaea.de/10.1594/PANGAEA.937781)
 465 [PANGAEA.937781](https://doi.pangaea.de/10.1594/PANGAEA.937781).
- 466 Koetz, B., Bastiaanssen, W., Berger, M., Defourny, P., Del Bello, U., Drusch, M., et
 467 al. (2018). High Spatio- Temporal Resolution Land Surface Temperature Mis-
 468 sion - a Copernicus Candidate Mission in Support of Agricultural Monitoring.
 469 In *Igarss 2018-2018 ieee international geoscience and remote sensing sympo-*
 470 *sium* (pp. 8160–8162). doi: <https://doi.org/10.1109/IGARSS.2018.8517433>
- 471 Krumpfen, T., Birrien, F., Kauker, F., Rackow, T., von Albedyll, L., Angelopou-
 472 los, M., ... others (2020). The MOSAiC ice floe: sediment-laden sur-
 473 vivor from the Siberian shelf. *The Cryosphere*, 14(7), 2173–2187. doi:
 474 <https://doi.org/10.5194/tc-14-2173-2020>
- 475 Landy, J., Ehn, J., Shields, M., & Barber, D. (2014). Surface and melt pond evo-
 476 lution on landfast first-year sea ice in the Canadian Arctic Archipelago. *Jour-*
 477 *nal of Geophysical Research: Oceans*, 119(5), 3054–3075. doi: [https://doi.org/](https://doi.org/10.1002/2013JC009617)
 478 [10.1002/2013JC009617](https://doi.org/10.1002/2013JC009617)
- 479 Light, B., Grenfell, T. C., & Perovich, D. K. (2008). Transmission and absorption of
 480 solar radiation by Arctic sea ice during the melt season. *Journal of Geophysical*
 481 *Research: Oceans*, 113(C3). doi: <https://doi.org/10.1029/2006JC003977>
- 482 Light, B., Smith, M. M., Perovich, D. K., Webster, M. A., Holland, M. M., Linhardt,
 483 F., ... others (2022). Arctic sea ice albedo: Spectral composition, spatial het-
 484 erogeneity, and temporal evolution observed during the MOSAiC drift. *Elem*
 485 *Sci Anth*, 10(1), 000103. doi: <https://doi.org/10.1525/elementa.2021.000103>
- 486 Nicolaus, M., Katlein, C., Maslanik, J., & Hendricks, S. (2012). Changes in Arctic
 487 sea ice result in increasing light transmittance and absorption. *Geophysical Re-*
 488 *search Letters*, 39(24). doi: <https://doi.org/10.1029/2012GL053738>
- 489 Nicolaus, M., Perovich, D. K., Spreen, G., Granskog, M. A., von Albedyll, L., An-
 490 gelopoulos, M., ... others (2022). Overview of the MOSAiC expedition: Snow
 491 and sea ice. *Elem Sci Anth*, 10(1), 000046. doi: [https://doi.org/10.1525/](https://doi.org/10.1525/elementa.2021.000046)
 492 [elementa.2021.000046](https://doi.org/10.1525/elementa.2021.000046)
- 493 Nixdorf, U., Dethloff, K., Rex, M., Shupe, M., Sommerfeld, A., et al. (2021). *MO-*
 494 *SAiC extended acknowledgement*. Zenodo [https://doi.org/10.5281/zenodo](https://doi.org/10.5281/zenodo.5541624)
 495 [.5541624](https://doi.org/10.5281/zenodo.5541624).
- 496 Perovich, D., Jones, K., Light, B., Eicken, H., Markus, T., Stroeve, J., & Lindsay, R.
 497 (2011). Solar partitioning in a changing arctic sea-ice cover. *Annals of Glaciol-*
 498 *ogy*, 52(57), 192–196. doi: <https://doi.org/10.3189/172756411795931543>
- 499 Petrich, C., Eicken, H., Polashenski, C. M., Sturm, M., Harbeck, J. P., Perovich,
 500 D. K., & Finnegan, D. C. (2012). Snow dunes: A controlling factor of melt
 501 pond distribution on Arctic sea ice. *Journal of Geophysical Research: Oceans*,
 502 117(C9). doi: <https://doi.org/10.1029/2012JC008192>
- 503 Polashenski, C., Perovich, D., & Courville, Z. (2012). The mechanisms of sea ice
 504 melt pond formation and evolution. *Journal of Geophysical Research: Oceans*,
 505 117(C1). doi: <https://doi.org/10.1029/2011JC007231>
- 506 Popović, P., Cael, B., Silber, M., & Abbot, D. S. (2018). Simple rules govern the
 507 patterns of Arctic sea ice melt ponds. *Physical review letters*, 120(14), 148701.

- 508 doi: <https://doi.org/10.1103/PhysRevLett.120.148701>
- 509 Rabe, B., Heuzé, C., Regnery, J., Aksenov, Y., Allerholt, J., Athanase, M., ... others
510 (2022). Overview of the MOSAiC expedition: Physical oceanography. *Elem Sci*
511 *Anth*, 10(1), 00062. doi: <https://doi.org/10.1525/elementa.2021.00062>
- 512 Scott, F., & Feltham, D. (2010). A model of the three-dimensional evolution of Arctic
513 melt ponds on first-year and multiyear sea ice. *Journal of Geophysical Re-*
514 *search: Oceans*, 115(C12). doi: <https://doi.org/10.1029/2010JC006156>
- 515 Shokr, M., & Sinha, N. (2015). *Sea ice: physics and remote sensing*. John Wiley &
516 Sons.
- 517 Shupe, M. D., Rex, M., Blomquist, B., Persson, P. O. G., Schmale, J., Uttal, T., ...
518 others (2022). Overview of the MOSAiC expedition: Atmosphere. *Elem Sci*
519 *Anth*, 10(1), 00060. doi: <https://doi.org/10.1525/elementa.2021.00060>
- 520 Thielke, L., Huntemann, M., Hendricks, S., Jutila, A., Ricker, R., & Spreen, G.
521 (2022a). *Helicopter-borne thermal infrared sea ice surface temperature maps*
522 *with 1 m resolution during the MOSAiC expedition, NetCDF format, version 2*.
523 PANGAEA. <https://doi.org/10.1594/PANGAEA.940846>.
- 524 Thielke, L., Huntemann, M., Hendricks, S., Jutila, A., Ricker, R., & Spreen, G.
525 (2022b). Sea ice surface temperatures from helicopter-borne thermal infrared
526 imaging during the MOSAiC expedition. *Scientific Data*, 9(1), 1–16. doi:
527 <https://doi.org/10.1038/s41597-022-01461-9>
- 528 Vihma, T., Pirazzini, R., Fer, I., Renfrew, I. A., Sedlar, J., Tjernström, M., ... oth-
529 ers (2014). Advances in understanding and parameterization of small-scale
530 physical processes in the marine Arctic climate system: a review. *Atmospheric*
531 *Chemistry and Physics*, 14(17), 9403–9450. doi: [https://doi.org/10.5194/](https://doi.org/10.5194/acp-14-9403-2014)
532 [acp-14-9403-2014](https://doi.org/10.5194/acp-14-9403-2014)
- 533 Webster, M. A., Holland, M., Wright, N. C., Hendricks, S., Hutter, N., Itkin, P.,
534 ... others (2022). Spatiotemporal evolution of melt ponds on Arctic sea ice:
535 MOSAiC observations and model results. *Elem Sci Anth*, 10(1), 000072. doi:
536 <https://doi.org/10.1525/elementa.2021.000072>